International Journal of Remote Sensing

ISSN: (Print) (Online) Journal homepage: www.tandfonline.com/journals/tres20

A comparative study on intra-annual classification of invasive saltcedar with Landsat 8 and Landsat 9

Ruixuan Li, Le Wang & Ying Lu

To cite this article: Ruixuan Li, Le Wang & Ying Lu (2023) A comparative study on intra-annual classification of invasive saltcedar with Landsat 8 and Landsat 9, International Journal of Remote Sensing, 44:6, 2093-2114, DOI: 10.1080/01431161.2023.2195573

To link to this article: https://doi.org/10.1080/01431161.2023.2195573

Published online: 11 Apr 2023.

INTERNATIONAL JOURNAL OF REMOTE SENSING
2023, VOL. 44, NO. 6, 2093–2114
https://doi.org/10.1080/01431161.2023.2195573

Taylor & Francis
Taylor & Francis Group

A comparative study on intra-annual classification of invasive saltcedar with Landsat 8 and Landsat 9

Ruixuan Li, Le Wang and Ying Lu

Department of Geography, University at Buffalo, Buffalo, NY, USA

ABSTRACT

The rapid expansion of exotic saltcedar along riparian corridors has dramatically altered the landscape structure and ecological function of riparian habitats in the western United States. The development of accurate and reproducible mapping methods with remote sensing plays an indispensable role in the timely monitoring of saltcedar, re-evaluating its ecological functions, and establishing effective control measures. The utmost challenge for achieving this goal is manifested as the lack of time series of remote sensing images to capture the saltcedar phenology adequately. To this end, the newly available Landsat 9 images, combined with its counterpart of Landsat 8, offer a precious opportunity to compensate for the temporal image shortage. To understand Landsat 9 in the saltcedar classification and to discover helpful information for its application, this study presents the first attempt to classify saltcedar using intra-annual Landsat 8 and Landsat 9 images. We adopted two machine learning algorithms, support vector machine (SVM) and random forest (RF), to compare the performance of Landsat 9 and Landsat 8 for intra-annual saltcedar classification. In addition, we investigated the respective contribution of each spectral band to the overall performance and identified the optimal time window for saltcedar classification. The results indicated that the difference in classification performance between Landsat 9 and Landsat 8 was insignificant. The shortwave infrared bands associated with both Landsat 8 & 9 have contributed most to the process of saltcedar identification. Image acquired in July, November, and December yielded better results than other months for saltcedar classification. It is concluded that Landsat 8 & 9 constellation has the potential to refine saltcedar classification accuracy on larger spatial and temporal scales.

ARTICLE HISTORY
Received 16 December 2022
Accepted 19 March 2023

1. Introduction

Saltcedar (*Tamarix* spp.), an exotic woody shrub introduced to the U.S. in the mid-1800s, has actively invaded the southwestern US by alternating the riparian zone vegetation composition, depleting water resources, changing the associated wildlife habitat, and decreasing biodiversity (Di Tomaso 1998; Friedman et al. 2005; Nagler et al. 2011, 2021). Since its first cultivation in California in 1856, this aggressive plant has expanded along the

CONTACT Le Wang lewang@buffalo.edu Department of Geography, University at Buffalo, 110 Wilkeson Quad Ellicott Complex, North Campus Buffalo, NY, USA

riparian corridor at a rate of 20 km per river reach per year (Graf 1978). It has not only significantly destructed the native vegetation but also profoundly altered the riparian ecosystem (Nagler et al. 2011). Along with the alternation, the remarkable water-consuming capability of saltcedar has exhausted the water resources, increased the salinity of the soil, and finally degraded the wildlife habitat quality where the saltcedar colonized (Di Tomaso 1998; Hart et al. 2005). Consequently, 93% of riparian wetland habitat has declined along the Rio Grande river compared to 1918, resulting in a significant decrease in populations of multiple riparian obligate species (Friggens and Finch 2015). Thus, to guide the effective control of this invasive species, a detailed map of saltcedar is not enough. Timely continuous monitoring of saltcedar is urgently required to track its distribution variation.

Remote sensing has greatly succeeded in monitoring the distribution of saltcedar in the past 30 years. The application of remote sensing to saltcedar research continues to evolve with the development of data. Aerial photographs were first applied to detect invasion patterns and spectral characteristics of saltcedar (Everitt and Deloach 1990; Everitt et al. 1996). Subsequently, the development of high-resolution aerial and satellite imagery has led to more accurate saltcedar distribution mapping for a single time (Diao and Wang 2014; Ji and Wang 2015; Silván-Cárdenas and Wang 2010; Wang and Zhang 2014; Yang, Everitt, and Fletcher 2013). However, due to limited spatial coverage and expensive acquisition costs, aerial and high-resolution images are difficult to achieve effective regional-scale saltcedar monitoring. Free and easily accessible moderate-resolution images provide an effective way to address this problem. The broad spatial and temporal coverage of the moderate resolution imagery allows mapping of saltcedar distribution and abundance over a larger area (Evangelista et al. 2009; Maruthi Sridhar et al. 2010) while quantifying changes in saltcedar evapotranspiration and leaf phenology due to the release of the biocontrol agent: saltcedar leaf beetles (*Diorhabda carinulata*) (Bateman, Nagler, and Glenn 2013; Ji, Wang, and Knutson 2017; Nagler et al. 2012). However, detecting the distribution of saltcedar by using single-scene Landsat images acquired at a specific time still faces challenges. Plants of different phenological stages may exist in a single image. The essential phenological features that facilitate the differentiation of saltcedar cannot be completely captured in a single observation (Diao and Wang 2016a). The development of timely monitoring methods based on long-time scale observations to fully utilize the information of phenological dynamics is an important approach to improve the accuracy of saltcedar distribution mapping.

The time series of Landsat imagery is suitable for capturing the phenological dynamics of invasive plants (Bradley 2014). The phenological bands detection strategy based on the Landsat monthly time series was proposed to adapt to the intra-annual phenological variation of saltcedar (Diao and Wang 2016a). Compared to the commonly used single-scene detection strategy, incorporating phenological bands largely increased the detection accuracy. The overall classification accuracy increased from 83.35% to 88.54%, and the Kappa coefficient rose from 0.71 to 0.80. The late autumn and early winter periods (October, November, and December) were discovered to be critical for riparian vegetation differentiation. In addition to intra-annual phenological change information, inter-annual leaf senescence of saltcedar can be predicted by the multiyear spectral angle clustering (MSAC) model (Diao and Wang 2018), which can guide the construction of synthetic images of Landsat surface reflectance products. Compared to the accuracies of the single-

date. image, the user's accuracy of the saltcedar increased by about 3% and the producer's accuracy of the saltcedar increased by 9% through using the composite image. On the other hand, to address the possible variation in phenological characteristics within saltcedar populations in single-date. images, the saltcedar colouration model was discovered (Ji and Wang 2016). The timing of saltcedar peak colouration is linearly correlated with the timing of leaf drop. This relationship can be modelled by the MODIS end-of-season time product (EoST) with Landsat images through a simple linear equation as a guide to determine the optimal date for each pixel to obtain Landsat images for saltcedar mapping. The result shows that the composite image based on phenology is more beneficial for saltcedar distinction than a single-scene image. However, the relatively coarse temporal resolution of previous Landsat products makes it difficult to obtain sufficient cloud-free imagery to develop a phenology-based detection strategy (Diao and Wang 2016a). The highly dynamic properties of saltcedar invasion may cause synthetic images generated under the guidance of the saltcedar colouration model or MSAC model to fail to produce robust classification results (Diao and Wang 2018; Ji and Wang 2016). There is an urgent need to incorporate new data to make the time series more intensive to satisfy the requirement for more effective and accurate timely monitoring of saltcedar and its co-occurring vegetation (Diao and Wang 2016a, 2018; Ji and Wang 2016).

The release of Landsat 9 provides new opportunities for constructing more intensive time series for saltcedar studies. Landsat 9 carries the Operational Land Imager-2 (OLI-2), which provides calibrated images, including solar reflectance wavelengths almost equivalent to the Landsat 8 OLI (Masek et al., 2020). The combined Landsat 8/9 constellation will provide an 8-day observation of the Earth. There have been numerous studies demonstrating that heterogenous image fusion can break through the limitations of the temporal resolution of a single data source (Bolton et al. 2020; Liu et al. 2020; Moon, Richardson, and Friedl 2021; Pan et al. 2021; Shen et al. 2021; Wang et al. 2020; Zhang et al. 2022). However, due to the differences in the sensors in orbit, space, and spectral configuration, the physical measurement value and radiation properties of the images will be affected. It is often necessary to select compatible bands in different datasets and perform appropriate coefficient transformations and resampling to unify remote sensing data to obtain comparable results (Graf 1978; Liu et al. 2020; Wang et al. 2020; Zhang et al. 2022). The same spatial resolution and similar band design of Landsat 9 and Landsat 8 make it possible to build a more intensive Earth observation system together without the need for complex data pre-processing. Landsat 9 has proven to produce outstanding results in land use and land cover classification, plant phenology estimation, and water quality retrieval (Guo et al. 2022; Niroumand-Jadidi et al. 2022; Shahfahad et al. 2022; You et al. 2022). However, the applicability of Landsat 9 data to saltcedar-related studies has not been investigated. The differences in performance between Landsat 9 and Landsat 8 for saltcedar classification need to be scientifically compared. The role played by different bands in saltcedar identification using OLI series sensors is unclear. More intensive time series may also bring new knowledge of the critical period for saltcedar classification. These issues need to be addressed for our in-depth understanding of the utilization of Landsat 8 & 9 constellation for accurate timely monitoring of saltcedar invasion and re-evaluation of its ecological functions in the future.

The overall objective of this study was to understand Landsat 9 in saltcedar classification. Specifically, we set up three objectives: (1) to compare the performance

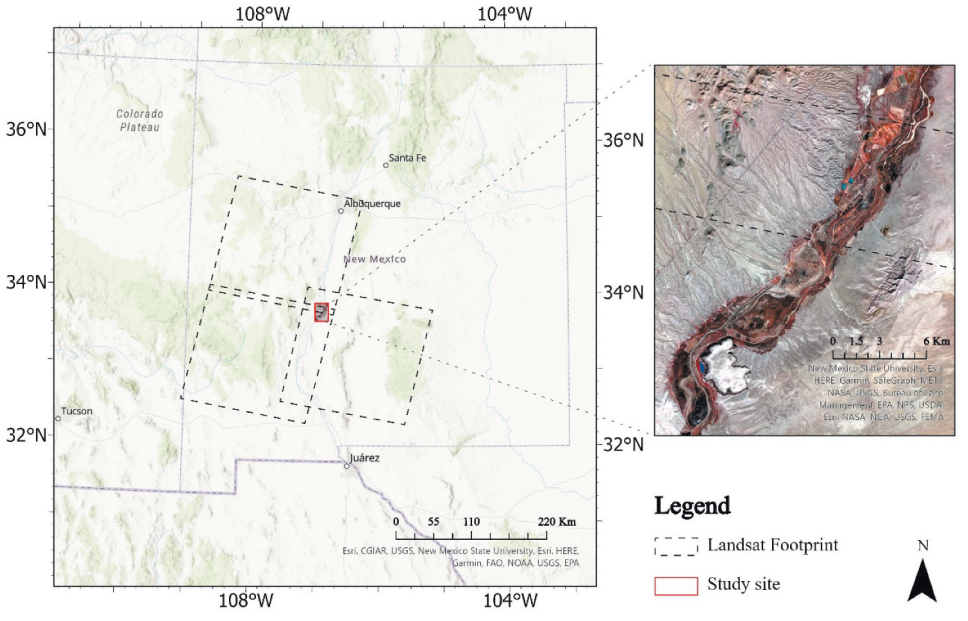

Figure 1. The geographic location of the study site with the preview of the false-colour composite of Landsat imagery on the right side.

of Landsat 9 V.S. Landsat 8 for intra-annual saltcedar classification; (2) to quantify the individual band contribution of Landsat 8 and Landsat 9; (3) to identify the intra-annual optimal time window for combining Landsat 8 and 9. We expect the results to provide a scientific foundation for data selection for the saltcedar remote monitoring while possessing the potential for generalization and replication to larger spatial and temporal scales.

2. Study site

The Rio Grande River originates from southern Colorado's San Juan Mountains and travels south to the Gulf of Mexico. It is one of the most regulated rivers in the southwestern US. The study site is near the town of San Antonio, New Mexico (33° 48′18″ N, 106°53′26″ W, 1375 m elev.), at the Middle Rio Grande River (Figure 1). The width of the riparian corridor is about 2 km. According to the description provided in earlier research, the climate at this study location is classified as dry to the south and semiarid to the north. Dense, single-species saltcedar dominates the riverbank.

3. Methods

Four major steps were followed in this research as summarized in Figure 2: (i) reference data preparation and image pre-processing, (ii) intra-annual saltcedar classification with Landsat 8 & 9, (iii) individual band contribution quantification, (iv) intra-annual optimal time window identification.

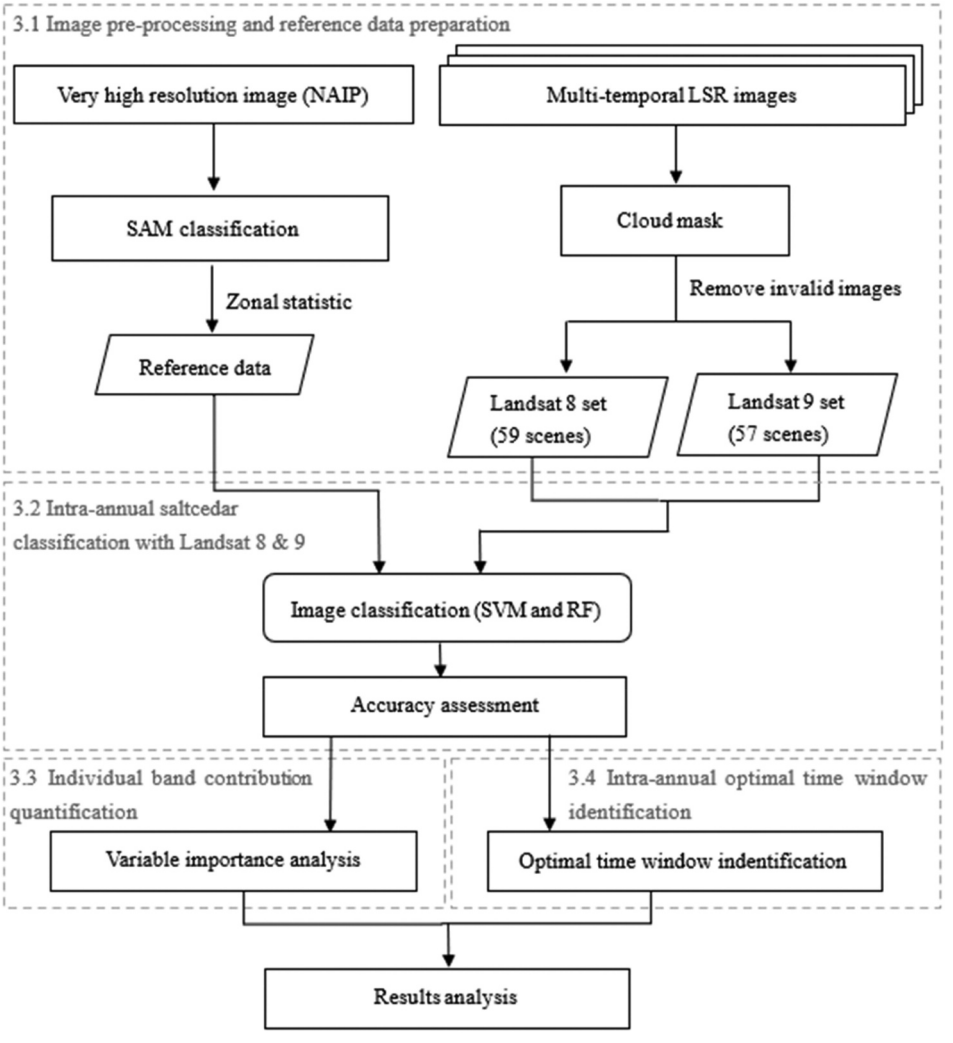

Figure 2. Flowchart of the methodology.

3.1. Image pre-processing and reference data preparation

3.1.1. Landsat time series data

To compare the performance of Landsat 9 and Landsat 8 for intra-annual saltcedar classification, all the LSR images from Nov.1, 2021, to Nov.1, 2022, were collected for Landsat 9 and Landsat 8, respectively. Initially, we acquired 66 Landsat 8 images and 65 Landsat 9 images that completely covered the study site. The de-clouding mask was then established in Google Earth Engine (GEE) for all LSR images in both Landsat 8 and Landsat 9 datasets. We excluded the images with more than 20% of cloud coverage. Finally, the remaining 59 Landsat 8 images and 57 Landsat 9 images were collected (Table 1). In addition, two typical vegetation indices, the normalized difference vegetation index (NDVI) and normalized difference water index (NDWI) (Diao and Wang 2016a; Gao 1996; Huang et al. 2021;

Table 1. Summary of LSR image data used in this study. The number in brackets represents the total number of scenes in the data series.

Satellite	Path and Row	Number of scenes
Landsat 8 (59)	p33r37	21
	p34r36	19
	p34r37	19
Landsat 9 (57)	p33r37	18
	p34r36	19
	p34r37	20

Pettorelli et al. 2005), were calculated for each image and involved them as candidate features for saltcedar classification.

3.1.2. Saltcedar reference data preparation

The saltcedar reference data, including training and validation samples, were prepared by resampling the classification result of an aerial image produced by the National Agriculture Image Program (NAIP). Since no NAIP image was available in 2021 and 2022, we selected the one acquired at the closest date, 2020, for this study. This NAIP image, at 0.6 m resolution with four spectral bands: blue, green, red, and near-infrared, was downloaded from the New Mexico Resource Geographic Information System (RGIS, http://rgis.unm.edu/). It was ready to use with image orthorectification.

The spectral angle mapper (SAM) was utilized to classify the NAIP image since it has been proven effective in saltcedar classification with high spatial resolution images (Narumalani et al. 2006). Thus, we believe SAM can help acquire reliable ground truth of saltcedar from the NAIP image. SAM identifies the similarity of the image spectra to the reference spectra in the spectral library by treating them as vectors in n-dimensional space and calculating the angle. The image spectra forming the smallest spectral angle are assigned to the corresponding category (Kruse et al. 1993). This technique is relatively insensitive to the effects of illumination and albedo when used for calibrated reflectance data. Additionally, in order to eliminate the errors caused by the time mismatch between the Landsat images and the NAIP image, high-resolution images in 2020, 2021, and 2022 on Google earth pro were used as references.

Then, the classification result of NAIP was resampled from 0.6 m to 30 m resolution using zonal statistics in order to produce reference data for the 30 m spatial resolution Landsat images. First, we used a 30 m grid to perform zonal statistics on the classification result. Then, 50% was set as the threshold to label each 30 m-by-30 m pixel as saltcedar (>50%) or non-saltcedar (<50%). At last, a total of 663 30 m-by-30 m pixels were labelled as saltcedar. A zoom-in view of the resultant reference data can be found in Figure 3. However, pixels with no saltcedar in their 3-by-3 neighbouring pixels were considered as salt and pepper errors since they have a high probability of being misclassified. After removing the salt and pepper errors, a total of 350 pixels were collected as saltcedar reference data. These reference data were randomly split into two parts: 80% were used to generate training samples, and the other 20% were used as validation samples for subsequent accuracy assessment of Landsat classification results.

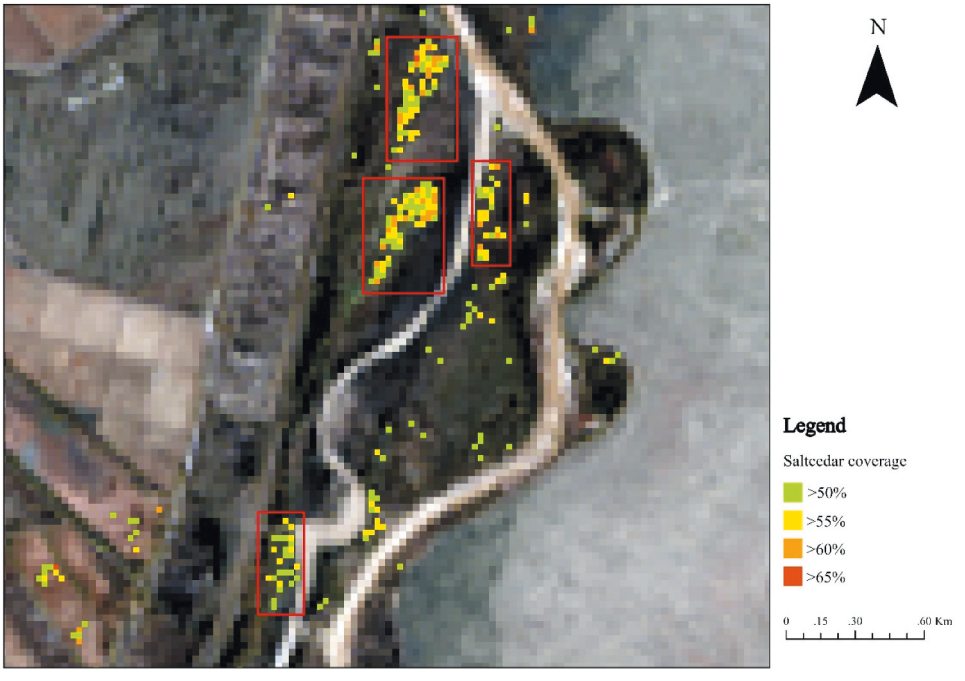

Figure 3. A zoom-in view of pixels with more than 50% coverage by saltcedar in zonal statistics. Pixels in the red box were selected as saltcedar reference data. The base image is an LSR product.

3.2. Intra-annual saltcedar classification with Landsat 8 & 9

To compare the performance of Landsat 9 and Landsat 8 on intra-annual saltcedar classification, we employed two machine learning algorithms that have been proven to achieve favourable results in both saltcedar classification and the classification of other land use and land cover types (Sheykhmousa et al. 2020): support vector machine (SVM) (Fletcher, Everitt, and Yang 2011; Ji and Wang 2015; Tai and Wang 2014; Wang and Zhang 2014; Xun and Wang 2015) and random forest (RF) (Diao and Wang 2016a, 2018). However, another algorithm commonly used in saltcedar classification: the spectral angle mapper (SAM) (Diao and Wang 2018; Silván-Cárdenas and Wang 2010), was not applied and discussed in this study due to the inability to conduct ground surveys to obtain sufficient information about the co-occurring species and their spectra. In addition, the performance of Landsat 8 and Landsat 9 with the two algorithms was investigated by evaluating the classification accuracy using confusion matrices.

3.2.1. Classification algorithms

SVM has been proven to be effective with a small amount of training samples and high-dimensional images (Pal and Mather 2005). It strives to find an optimal hyperplane that maximizes the margin between two classes based on the support vectors, defined as each class's nearest vector to the hyperplane. The initial linear SVM assumes that the multi-dimensional data are linearly separable, but the sample data often overlap in practice. Therefore, a kernel function is introduced to project the input data into a higher dimensional space to construct the hyperplane. We used the radial basis function (RBF) as the

kernel function because it is the most commonly used kernel function for classifying remote sensing images and has the best performance in saltcedar classification (Ji and Wang 2015; Tai and Wang 2014; Wang and Zhang 2014; Xun and Wang 2015). When using RBF as the kernel function, it is inevitable to define two critical parameters, γ and C. Where γ represents the range of influence of a particular training sample in the high-dimensional space and C indicates the tolerance of the model to misclassification. Referring to the previous study on saltcedar classification with SVM (Wang and Zhang 2014), the grid search method was applied to determine the optimal γ and C (Hsu, Chang, and Lin 2003). We first defined the lower bounds for γ and C and independently increased them at each step up to the upper bounds at an exponential pace ($\gamma \in [2^{-5}, 2^{3}]$, $C \in [2^{-3}, 2^{5}]$, specifically). Then we compared the overall accuracies obtained by SVM with different combinations of γ and C for a total of eight test images (four for Landsat 8 and four for Landsat 9, acquired at close dates in March, June, September, and December, respectively). The results suggested that the highest overall classification accuracy could be achieved when $\gamma = 8$, $C = 32$ for all test images. Therefore, we applied the SVM constructed with $\gamma = 8$, $C = 32$ to classify all Landsat images acquired in this study.

A random forest (RF) is an ensemble of a number of decision trees. The construction of each decision tree is based on randomly selected features of the training samples (Breiman 2001). As an ensemble method, RF is robust to small changes in the input data and insensitive to noise. In addition, RF is able to process thousands of candidate features simultaneously and measure the importance of each candidate feature since it does not require dimensionality reduction of the data, making it one of the ideal classification methods for saltcedar classification (Diao and Wang 2016a). The ability of the random forest to evaluate the variable importance measures (VIMs) is also an important reason for choosing it as one of our classification algorithms, which can provide the basis for the subsequent quantification of individual band contribution. To run the RF model, two parameters must be set: the number of randomly selected features (Mtry) and the number of trees (Ntree). In this study, Mtry was set to the square root of the total number of features, which is the most recommended value (Sheykhmousa et al. 2020). The number of decision trees (Ntree) for RF was set to 100. This number was derived by the following two steps: we first trained the RF model consisting of 50 decision trees using training samples, then used this model to pre-classify the Landsat 8 and Landsat 9 datasets. Images with the highest overall classification accuracy of both datasets were extracted for testing the effect of the number of decision trees in the interval from 5 to 200 with a step size of 5. The result indicated that two images achieved the highest overall accuracy when the number of decision trees was 100. Therefore, all images were reclassified using an RF model containing 100 decision trees.

3.2.2. Accuracy assessment

The confusion matrix was constructed for each classification result with validation samples. Four accuracy metrics: overall Accuracy (OA), Kappa coefficients, producer's accuracy (PA), user's accuracy (UA), and F-1 score, were calculated from the confusion matrix. Among them, the saltcedar producer's accuracy, the saltcedar user's accuracy, and Kappa coefficients are the most frequently used metrics in the subsequent analysis because the saltcedar producer's accuracy and the saltcedar user's accuracy are intuitive representations of saltcedar classification results (Diao and Wang 2016a, 2016b; Ji and

Wang 2016; Ji, Wang, and Knutson 2017; Wang et al. 2013), while the kappa coefficient considers all elements of the confusion matrix and better reflects the consistency of classification results with the reality than overall accuracy (Fung and LeDrew 1988). The F-1 score was also calculated to compare the comprehensive performance of the two datasets in saltcedar classification. In addition, since the LSR images of path 34 row 36 and path 34 row 37 covered the whole study area and were acquired at the same time, we selected the images with relatively higher saltcedar user's accuracy for the subsequent analysis.

3.3. Individual band contribution quantification

The individual band contribution for saltcedar classification was quantified by the feature important analysis with variable importance measurement (VIM) carried by the RF classification algorithm. The RF classification results with the highest overall accuracy were selected for VIM in Landsat 8 and Landsat 9, respectively. The VIM was accomplished by the 'ee. Classifier. explain' function in GEE. This function uses the mean decrease in Gini (MDG) to quantify the importance of different variables, defined as the total decrease in node impurities from splitting on the variable, averaged over all trees (Han, Guo, and Yu 2016). If a variable is important to the classification result, it tends to split mixed labelled nodes into pure single-class nodes. The higher quantity of pure nodes produced after splitting, the greater the total impurities reduction and the corresponding MDG. For each variable, i.e. the individual band used for the classification, the higher this mean value was, the greater the impact on classification accuracy when this band was changed, as well as the higher importance.

It should be noted that only the RF was used for feature importance analysis in this study. This is because the classification performance of SVM can benefit from feature importance derived by RF (Löw et al. 2013). The feature importance ranking generated by RF can guide the input feature selection of the SVM algorithm, thus improving the overall accuracy of the SVM based on the reduction of feature redundancy. In addition, the RF-based feature selection technique has the advantage of less training time while providing comparable performance to the SVM-based feature selection technique (Pal 2006). Therefore, we believe that feature importance analysis using RF to quantify the contribution of the individual band in saltcedar classification is representative and generalizable.

3.4. Intra-annual optimal time window identification

The classification results of Landsat 8 and Landsat 9 images after accuracy assessment in Section 3.2.2 were arranged and integrated in order of image acquisition time for the whole year to identify the intra-annual optimal time window for saltcedar classification. The Kappa coefficients for the classification results in this dataset were then aggregated month by month. In addition, their medians were calculated for each month. Larger Kappa coefficients and medians represent higher classification accuracy of LSR images obtained in that month. Thus this month was defined as the best time window. Although in previous studies, late fall and early winter were considered the optimal time window because saltcedar at this stage has a characteristic orange-yellow colour that better distinguishes it from co-occurring vegetation (Diao and Wang 2016a; Evangelista et al.

2009; Ji and Wang 2016; Narumalani et al. 2006; Silván-Cárdenas and Wang 2010; Wang et al. 2013; Yang, Everitt, and Fletcher 2013). However, a more intensive time series consisting of Landsat 8 and Landsat 9 together may bring new knowledge on the optimal time window for saltcedar classification and provide more options in terms of data acquisition time. In addition, the distribution of kappa coefficients for each month can describe the robustness of saltcedar classification with different algorithms in different periods.

4. Results

4.1. Comparison of Landsat 8 & 9 in intra-annual saltcedar classification

The performance of Landsat 9 and Landsat 8 for intra-annual saltcedar classification was first compared by averaging five accuracy metrics of all classification results (Figure 4). For Landsat 9, the average overall classification accuracy obtained with the SVM classification algorithm was 0.92, the average Kappa coefficient was 0.89, and the corresponding average producer's accuracy, user's accuracy, and F-1 score of saltcedar were 0.86, 0.98, and 0.91, respectively. The average overall accuracy, average saltcedar producer's accuracy, average kappa coefficient, and average F-1 score obtained with RF classification algorithm are higher than those of SVM, which are 0.93, 0.90, 0.91, and 0.93, respectively. However, the average saltcedar user's accuracy yielded from the RF classification algorithm (0.97) is lower than that of SVM (0.98). The classification results of Landsat 8 exhibit similar patterns among the five average accuracy metrics. Regardless of the classification algorithm used, the difference between the average of the five metrics for Landsat 9 and Landsat 8 was insignificant (maximum difference of 0.01). Our results indicated that Landsat 9 performs consistently with Landsat 8 for intra-annual saltcedar classification and is independent of the choice of the classification algorithm.

The line graphs generated chronologically from image-by-image revealed the reasons for the similar average accuracy metrics achieved by Landsat 9 and Landsat 8 across the year (Figure 5). Regardless of which classification algorithm was used, the classification results obtained by Landsat 9 and Landsat 8 presented a high degree of overlap and similar trends on the time scale, especially on the

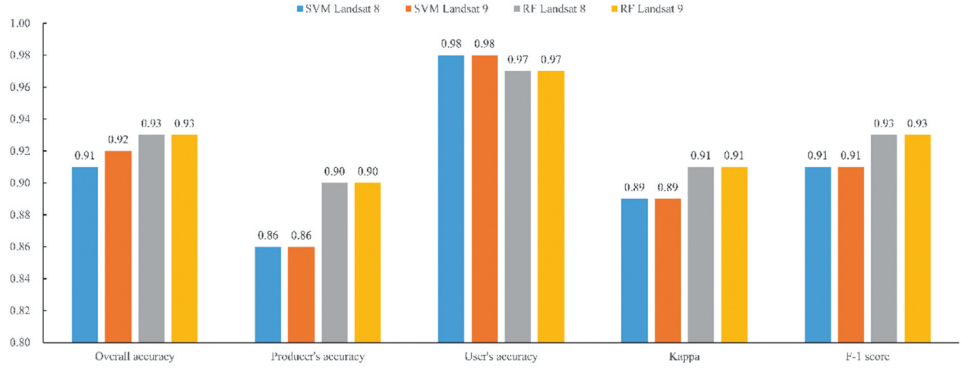

Figure 4. Average accuracy metrics of Landsat 8 & 9 classification results.

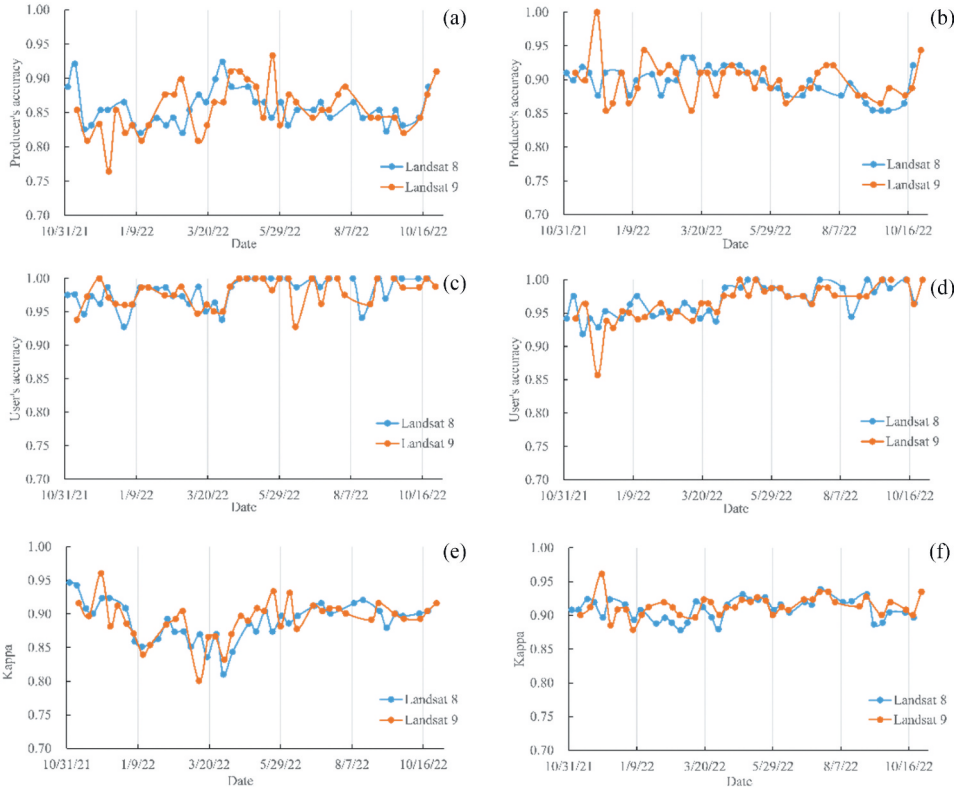

Figure 5. Three accuracy metrics for classification results produced by using the same algorithm for different datasets: (*a*) saltcedar producer's accuracy by SVM; (*b*) saltcedar producer's accuracy by RF; (*c*) saltcedar user's accuracy by SVM; (*d*) saltcedar user's accuracy by RF; (*e*) Kappa coefficient by SVM; (*f*) Kappa coefficient by RF.

saltcedar user's accuracies and Kappa coefficients. In addition, RF outperformed SVM in terms of saltcedar producer's accuracy and Kappa coefficients for both datasets. In contrast, more than 54% of the saltcedar user's accuracies produced by SVM were higher than those of RF (Figure 6). This indicated that using RF for classification can better avoid the omission of saltcedar pixels, while using SVM can reduce the probability of saltcedar pixels being misclassified as other land cover types.

4.2. Contribution of individual band to saltcedar classification

Two shortwave infrared bands (SR_B6 and SR_B7) contribute more to the saltcedar classification. The importance of the sixth band (SR_B6, SWIR 1, wavelength 1.57–1.65 μm) is the most prominent, 43.5% higher than the green band, which has the lowest contribution. The contribution of the same individual bands in the saltcedar classification of Landsat 9 is identical to that of Landsat 8. Different bands contribute to the saltcedar classification at different levels (Figure 7). Each band of the Landsat 8 and Landsat 9 products contains valuable information for saltcedar classification.

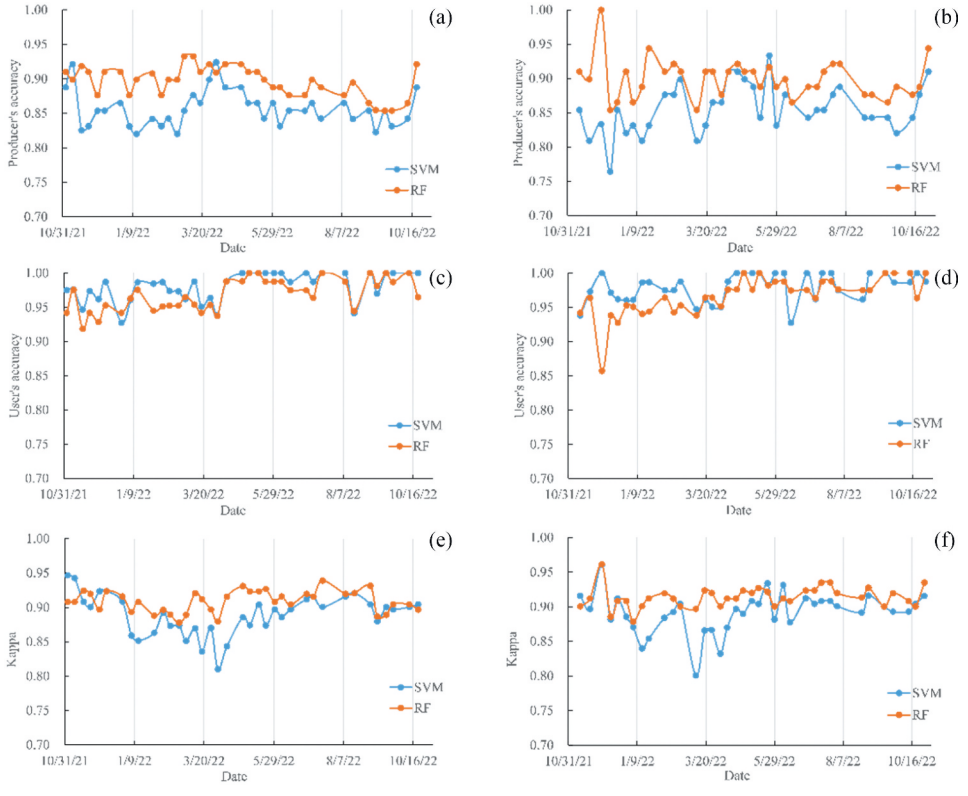

Figure 6. Three accuracy metrics for classification results produced by using different algorithms for the same dataset: (*a*) saltcedar producer's accuracy of Landsat 8; (*b*) saltcedar producer's accuracy of Landsat 9; (*c*) saltcedar user's accuracy of Landsat 8; (*d*) saltcedar user's accuracy of Landsat 9; (*e*) Kappa coefficient of Landsat 8; (*f*) Kappa coefficient of Landsat 9.

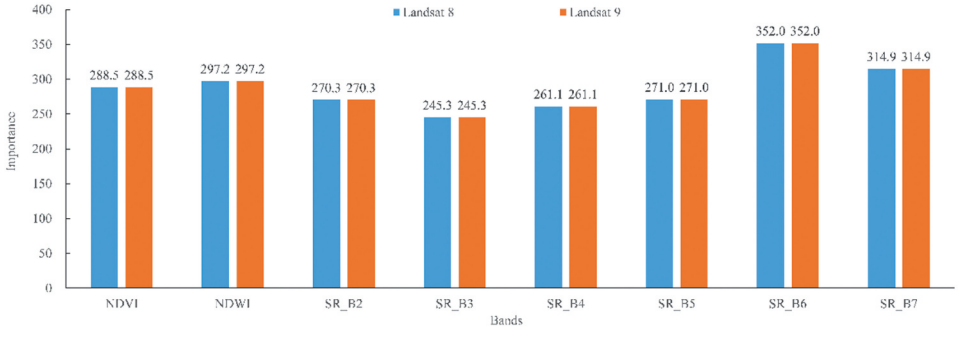

Figure 7. Variable importance of RF classification in Landsat 8 and Landsat 9 datasets.

It should be noted that NDVI and NDWI bands contribute more to the saltcedar classification than the visible and near-infrared bands. As a result, the incorporation of NDVI and NDWI bands for classification improved the annual average of all accuracy metrics for RF classification results (Figure 8), but the maximum improvement was only 0.02.

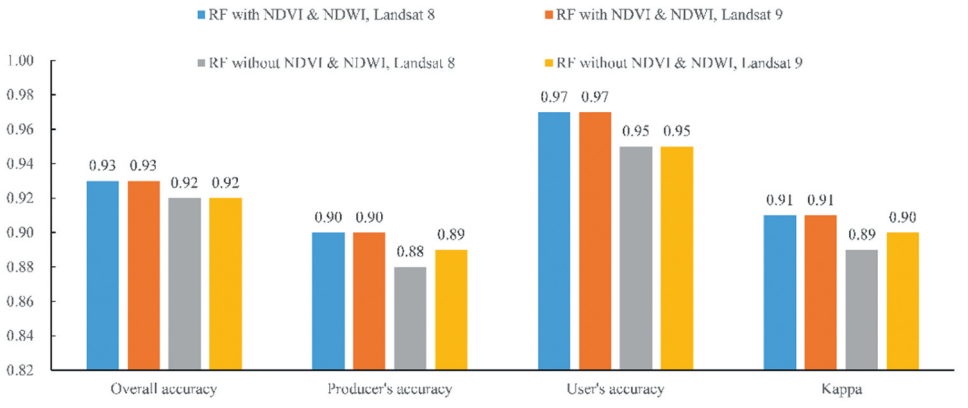

Figure 8. Comparison of RF classification results with and without the inclusion of NDVI and NDWI as classification features.

4.3. Optimal months for saltcedar classification

The optimal time window for saltcedar classification was investigated by summarizing the Kappa coefficients from the classification results of SVM and RF month by month. Our results indicated that the SVM-based saltcedar classification exhibits considerable monthly differences. November to December is the optimal time window for saltcedar classification with SVM in the study area. The median values of Kappa coefficients for these two months are the highest at 0.91, which is 0.05 higher than the lowest month (January, 0.86) (Figure 9). In addition to January, the classification results for March and April are also unfavourable. The

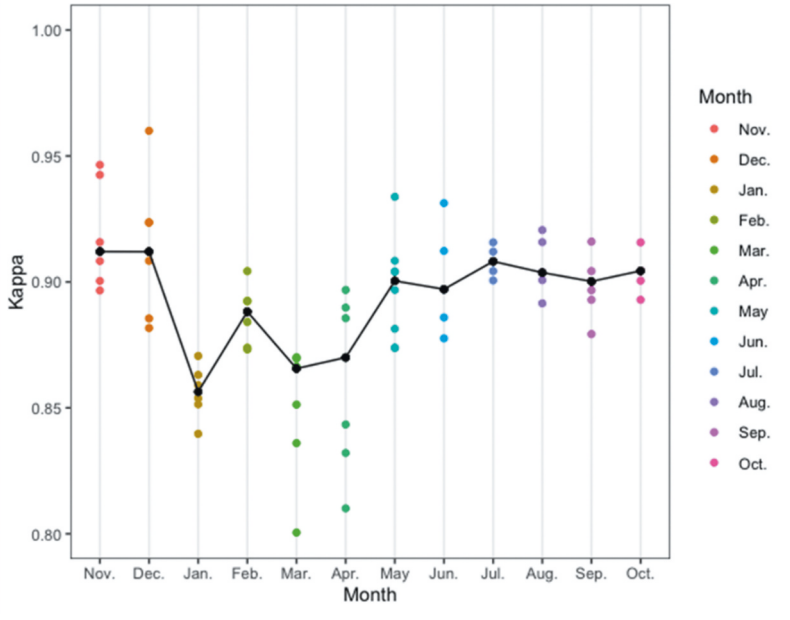

Figure 9. Individual value plots of Kappa coefficients based on SVM classification results. The black spots stand for the median value of each month.

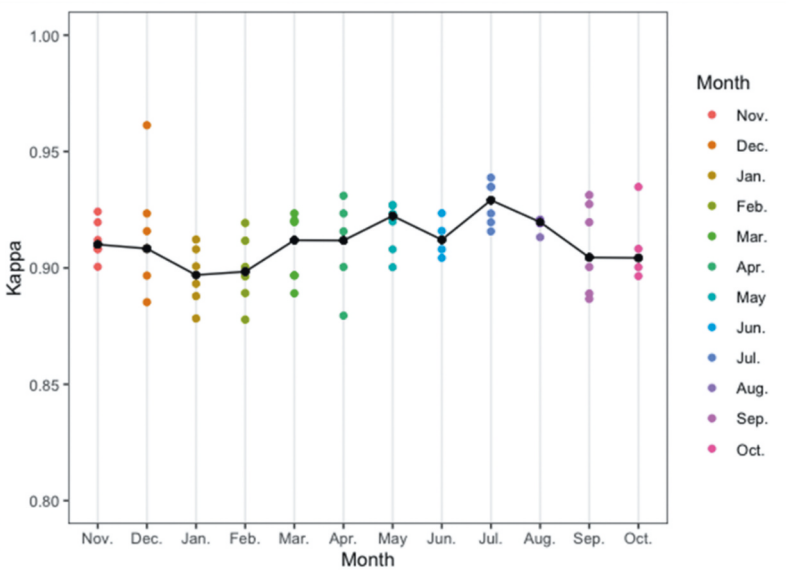

Figure 10. Individual value plots of Kappa coefficients based on RF classification results. The black spots stand for the median value of each month.

median values of the Kappa coefficients of these two months are relatively low and the intra-month distribution of them is also dispersed with a maximum variation of 0.09, indicating that the classification results of the images acquired in these two months are inconstant. The RF-based classification results are less affected by the image acquisition time. July is the optimal time window for saltcedar classification with RF in the study area, with a median Kappa coefficient of 0.93. Both intra-month and inter-month classification results exhibit robustness. The maximum difference between Kappa coefficients within the same month is 0.07. The median values of monthly Kappa coefficients are all above 0.90, and the difference between the maximum and the minimum median values is 0.03. The maximum difference in median values between the two adjacent months was even more negligible (0.02) (Figure 10).

Although the optimal months for the two classification algorithms, SVM and RF, to be used for saltcedar classification are different, this does not indicate that the optimal time windows for the different classification algorithms are entirely independent. For example, July is the only month which all the Kappa coefficients produced by the SVM exceeded 0.90. This indicated that it is feasible to obtain accurate results for saltcedar classification using SVM in July. In addition, both SVM and RF yielded the best Kappa coefficient (0.96) on 4 December 2021. This implied that the best saltcedar classification results could be obtained for images acquired in early December. In conclusion, our results revealed that July, November, and December are crucial months for saltcedar classification using the Landsat time series and can be used as optimal time windows.

5. Discussion

The newly available Landsat 9 images, combined with its counterpart of Landsat 8, offer a precious opportunity to compensate for the temporal image shortage. In

this study, we compared the intra-annual classification performance of Landsat 9 and Landsat 8 by adopting SVM and RF. The results indicated that there is no significant difference in the performance of Landsat 9 in intra-annual saltcedar classification compared to Landsat 8. The comparison of the classification results also revealed differences in the performance of the two algorithms. In addition, we quantified the contribution of the individual band to saltcedar classification and identified the optimal time window for intra-annual saltcedar classification using Landsat 8 & 9 constellation. Our findings suggested that the more intensive time series constructed by combining Landsat 8 & 9 has the potential to improve the accuracy of saltcedar classification further. To our knowledge, this study presented the first attempt at classifying saltcedar over the course of an entire year with Landsat 9 images.

5.1. Merits of saltcedar classification with Landsat 9

Landsat 9 images, while obtaining promising single-scene saltcedar classification accuracy, can be combined with Landsat 8 to construct a more intensive time series to improve the timely monitoring efficiency of saltcedar and capture more comprehensive information on saltcedar dynamics in the future.

The results of our study indicated that the classification performance of Landsat 8 & 9 for saltcedar is largely identical. This finding is consistent with the conclusions of studies on land use and land cover classification with Landsat 9 (Shahfahad et al. 2022; You et al. 2022). Regardless of the classification algorithm used, Landsat 8 and Landsat 9 yielded similar classification results. This can be attributed to the fact that Landsat 9 is equipped with an almost equivalent OLI-2 sensor as the Landsat 8 OLI (Masek et al., 2020). Therefore, the constellation system of Landsat 8 & 9 can be employed as a comprehensive, 30-metre spatial resolution and 8-day temporal resolution data source to construct a more intensive time series, doubling the amount of available data. The increase in the number of available images will promote the construction of a more intensive time series, enabling remote observations to more easily locate characteristic phenology information that is conducive to distinguishing saltcedar and thus improving classification accuracy (Diao and Wang 2016a, 2016b, 2018; Ji and Wang 2016). For example, the saltcedar peak colouration model proposed by Ji and Wang (2016) is based on the principle of selecting the Landsat image closest to the characteristic saltcedar phenology for each pixel, thus improving the discrimination of saltcedar. It can be envisaged that as the time series become more intensive, we will have more images available of specific areas, which may enable our approaching or covering the distinct phenological periods of saltcedar.

More intensive time series will also contribute to our ability to track and identify phenological changes in specific vegetation. The 16-day temporal resolution of the previous Landsat products has been argued to be unable to fully exploit the potential of some vegetation indices (e.g. NDVI) in describing plant phenology (Diao and Wang 2016a). More intensive observations make it possible to map phenology at a finer spatial scale and over a larger area (Gao and Zhang 2021) and determine the optimal vegetation indices for vegetation mapping at different phenophases (Guo et al. 2022). For example, in another study by Diao and Wang (2016b), the phenological process of saltcedar from leaf growth to leaf drop (i.e. leaf senescence process) was simulated using multi-temporal

spectral features. This multi-temporal spectral feature will become more accurate with the densification of time series.

It should be noted that the reason why the higher radiometric resolution of Landsat 9 than Landsat 8 was not outstanding in the saltcedar classification of this study is unclear. Landsat 9 can differentiate 16,384 shades of a given wavelength with the higher radiometric resolution. In comparison, Landsat 8 provides 12-bit data and 4,096 shades (Masek et al., 2020). The advanced design for radiation information acquisition makes Landsat 9 spacecraft could downlink the full 14 bits-per-pixel from OLI-2, rather than the 12 bits currently downlinked by Landsat 8, allowing sensors to detect more subtle differences, especially over darker areas such as water or dense forests. We assume that because the study site is a mixed stand of woody species dominated by saltcedar (Hamilton et al. 2019), the absence of dense canopy shade prevents Landsat 9 from fully exploiting its advantage of providing information in the dark area. On the other hand, it has been proven that there is a sizable intra-scene variation in the phenology of saltcedar. With the change in environmental conditions, such as latitude and the distance to water resources, the saltcedar in the same region may be in different phenological stages at the same time (Ji and Wang 2016). The impact of this intra-scene variation on the classification performance of Landsat 9 needs to be further investigated in the future.

5.2. Selection of the classification algorithm

The pixel-level classification performance of two machine learning algorithms that have proven to have outstanding capabilities in saltcedar monitoring: SVM and RF, were compared in this study. Although both algorithms obtain remarkable classification accuracy for the same images, the results show the advantages and disadvantages of each algorithm. For example, RF outperforms SVM in saltcedar producer's accuracy, while SVM is superior in saltcedar user's accuracy. In other words, RF would be a better choice if the objective is to avoid missing pixels of saltcedar, while SVM can better satisfy the requirement of preventing saltcedar from being misclassified as other land cover types and improving the accuracy in fieldwork.

Differences between the classification performance of SVM and RF affected by image acquisition time were observed on long-time scales. Although the input candidate features are the same for both classification models, the randomness of the features and samples of RF makes it insensitive to spectral differences in the same land cover type due to the different times of image acquisition. This can also be reflected in the more concentrated Kappa distribution of multiple images acquired within the same month using the RF classifier. SVM emphasizes the linear differentiability between each feature. When the spectral difference between saltcedar and co-occurring vegetation is relatively small (e.g. they have completely defoliated), the classification accuracy will be reduced accordingly. At the same time, the variation trend exhibited by SVM classification results can reflect the change of vegetation phenology in the study area to some extent. For example, the better classification results obtained by SVM in November may be due to the completion of the peak colouration of the saltcedar in the study area, turning it into a distinctive orange-yellow colour that allows it to be better distinguished from the co-occurring vegetation. Therefore, we suggest observing the distinct stages of plant life-cycle using SVM when conducting a study under phenological guidance is easier. On the

other hand, the robustness of RF makes it possible to identify saltcedar at any period without worrying about excessive degradation of classification accuracy due to the limitation of data acquisition time.

It should be emphasized that the classification and accuracy comparisons were performed separately for each Landsat 8 and Landsat 9 image in this study. Since the training and test samples for classification were collected separately for each image using the reference data preparation method (refer to Section 3.1.2), the samples are independent from each other for each image. Therefore, it is difficult to apply statistical tests to compare the performance of SVM and RF and draw consistent or comparable conclusions. However, we strongly recommend applying rigorous statistical tests to compare the performance of classifiers, such as the nonparametric McNemar test, when generating thematic classification maps containing extended timescale information in the future, thus avoiding accuracy metric errors caused by classification methods (Diao and Wang 2016a, 2018; Foody 2004; Park et al. 2018; Phan, Kuch, and Lehnert 2020; Schmidt et al. 2014).

5.3. Important bands for saltcedar classification

The shortwave infrared band (SWIR) played an important role in saltcedar classification. The extensive spread of biocontrol agents is probably the major reason for the prominent contribution of the shortwave infrared band. Saltcedar tends to form a continuous dense cover on the riparian corridor. The intra-annual saltcedar defoliation events can be induced due to the release of saltcedar leaf beetles (Nagler et al. 2021). This can lead to the frequent presence of non-photosynthetic material in saltcedar habitats, allowing for a corresponding spectral response in the shortwave infrared bands, leading to a prominent contribution of this feature in the classification. Previous studies have revealed that the SWIR sensing capabilities of WorldView-3 increase the classification accuracy of tropical tree species by allowing the detection of canopy non-photosynthetic materials (Ferreira et al. 2016). The defoliation of the species favoured the detection of non-photosynthetic material (branches and litter), which produced variations in the SWIR reflectance (Ferreira et al. 2019). In other words, SWIR potentially carries important information indicating the ecological impact of existing saltcedar control strategies, which needs further investigation. In addition, NDVI and NDWI bands did not significantly enhance the classification results. Exploiting phenological information to guide the construction of classification features may be an effective approach to improve classification performance further. For example, The detection strategy based on the phenological bands can carry rich phenological and spectral information of plants throughout the growing season and significantly improve the plant identification capability of Landsat products (Diao and Wang 2016a).

5.4. Optimal time window for saltcedar classification

In addition to November and December, which are consistent with the results of previous studies, we found that July is also an effective time window for saltcedar classification in the study area. Both classifiers produced robust classification results in July. All the Kappa coefficients obtained by SVM exceeded 0.90 in July, with the

most concentrated distribution. The RF algorithm produced the best classification results in July throughout the year. This new finding can be associated with the discussion in Section 5.3. Studies have demonstrated that saltcedar leaf beetles remain active in the late growing season of saltcedar and that their populations will have more time to increase in size from midsummer to late summer, resulting in more frequent saltcedar defoliation (Bean, Dalin, and Dudley 2012). The defoliation events have altered the original phenological patterns of saltcedar and might lead to the generation of new spectral information that facilitates the classification. We admitted that there are limitations in analysing the optimal time window for saltcedar classification in monthly terms. Our results indicated that the peak colouration of saltcedar in the study area probably occurs between November and December. Under these circumstances, further identification of the time interval in which the saltcedar phenological stage changes could help to improve the classification performance.

6. Conclusion

The incorporation of new data to support accurate and timely monitoring of saltcedar is urgently needed to re-evaluate the ecological impacts of exotic saltcedar in riparian habitats. In this study, we compared the performance of Landsat 8 and Landsat 9 for intra-annual saltcedar classification with two effective machine learning algorithms. Our results indicated no significant difference in the performance between Landsat 9 and Landsat 8 for intra-annual saltcedar classification in the study area. Landsat 8 & 9 constellation has the potential to refine saltcedar mapping because it can construct more intensive time series without the necessity of complex data pre-processing. The individual band contribution in saltcedar classification was also explored and we found that the shortwave infrared band plays a vital role in both Landsat 8 and Landsat 9. This could be associated with the intra-annual multiple defoliation events in saltcedar due to the release of biocontrol agents, which needs further investigation. In addition, we identified July as a novel month suitable for saltcedar classification besides November and December. In general, Landsat 9 imagery provides an unprecedented opportunity to facilitate the classification and timely monitoring of saltcedar at larger spatial and temporal scales, providing fundamental knowledge for understanding large-scale biological invasions and their response to climate change.

Acknowledgements

This work is supported by the National Science Foundation (Award # 1951657).

Disclosure statement

No potential conflict of interest was reported by the authors.

Funding

The work was supported by the National Science Foundation [1951657]

Data availability statement

The code and data that support the findings are available on Google Earth Engine with the following URLs: https://code.earthengine.google.com/24e8fd76b97cc26c4ef0da802522aa58 (SVM); https://code.earthengine.google.com/01ff46032bf5f4ca4dad9d91b8b7c5b2 (Random Forest).

References

Bateman, H., P. L. Nagler, and E. Glenn. 2013. "Plot-And Landscape-Level Changes in Climate and Vegetation Following Defoliation of Exotic Saltcedar (Tamarix Sp.) from the Biocontrol Agent Diorhabda Carinulata Along a Stream in the Mojave Desert (USA)." *Journal of Arid Environments* 89: 16–20. doi:10.1016/j.jaridenv.2012.09.011.

Bean, D. W., P. Dalin, and T. L. Dudley. 2012. "Evolution of Critical Day Length for Diapause Induction Enables Range Expansion of Diorhabda Carinulata, a Biological Control Agent Against Tamarisk (Tamarix Spp.)." *Evolutionary Applications* 5 (5): 511–523. doi:10.1111/j.1752-4571.2012.00262.x.

Bolton, D. K., J. M. Gray, E. K. Melaas, M. Moon, L. Eklundh, and M. A. Friedl. 2020. "Continental-Scale Land Surface Phenology from Harmonized Landsat 8 and Sentinel-2 Imagery." *Remote Sensing of Environment* 240: 111685. doi:10.1016/j.rse.2020.111685.

Bradley, B. A. 2014. "Remote Detection of Invasive Plants: A Review of Spectral, Textural and Phenological Approaches." *Biological Invasions* 16 (7): 1411–1425. doi:10.1007/s10530-013-0578-9.

Breiman, L. 2001. "Random Forests." *Machine Learning* 45 (1): 5–32. doi:10.1023/A:1010933404324.

Diao, C., and L. Wang. 2014. "Development of an Invasive Species Distribution Model with Fine-Resolution Remote Sensing." *International Journal of Applied Earth Observation and Geoinformation* 30: 65–75. doi:10.1016/j.jag.2014.01.015.

Diao, C., and L. Wang. 2016a. "Incorporating Plant Phenological Trajectory in Exotic Saltcedar Detection with Monthly Time Series of Landsat Imagery." *Remote Sensing of Environment* 182: 60–71. doi:10.1016/j.rse.2016.04.029.

Diao, C., and L. Wang. 2016b. "Temporal Partial Unmixing of Exotic Salt Cedar Using Landsat Time Series." *Remote Sensing Letters* 7 (5): 466–475. doi:10.1080/2150704X.2016.1149250.

Diao, C., and L. Wang. 2018. "Landsat Time Series-Based Multiyear Spectral Angle Clustering (MSAC) Model to Monitor the Inter-Annual Leaf Senescence of Exotic Saltcedar." *Remote Sensing of Environment* 209: 581–593. doi:10.1016/j.rse.2018.02.036.

Di Tomaso, J. M. 1998. "Impact, Biology, and Ecology of Saltcedar (Tamarix Spp.) in the Southwestern United States." *Weed Technology* 12 (2): 326–336. doi:10.1017/S0890037X00043906.

Evangelista, P. H., T. J. Stohlgren, J. T. Morisette, and S. Kumar. 2009. "Mapping Invasive Tamarisk (Tamarix): A Comparison of Single-Scene and Time-Series Analyses of Remotely Sensed Data." *Remote Sensing* 1 (3): 519–533. doi:10.3390/rs1030519.

Everitt, J., and C. Deloach. 1990. "Remote Sensing of Chinese Tamarisk (Tamarix Chinensis) and Associated Vegetation." *Weed Science* 38 (3): 273–278. doi:10.1017/S0043174500056526.

Everitt, J. H., D. E. Escobar, M. A. Alaniz, M. R. Davis, and J. V. Richerson. 1996. "Using Spatial Information Technologies to Map Chinese Tamarisk (Tamarix Chinensis) Infestations." *Weed Science* 44 (1): 194–201. doi:10.1017/S0043174500093759.

Ferreira, M. P., F. H. Wagner, L. E. Aragão, Y. E. Shimabukuro, and C. R. de Souza Filho. 2019. "Tree Species Classification in Tropical Forests Using Visible to Shortwave Infrared WorldView-3 Images and Texture Analysis." *Isprs Journal of Photogrammetry and Remote Sensing* 149: 119–131. doi:10.1016/j.isprsjprs.2019.01.019.

Ferreira, M. P., M. Zortea, D. C. Zanotta, Y. E. Shimabukuro, and C. R. de Souza Filho. 2016. "Mapping Tree Species in Tropical Seasonal Semi-Deciduous Forests with Hyperspectral and Multispectral Data." *Remote Sensing of Environment* 179: 66–78. doi:10.1016/j.rse.2016.03.021.

Fletcher, R. S., J. H. Everitt, and C. Yang. 2011. "Identifying Saltcedar with Hyperspectral Data and Support Vectormachines." *Geocarto International* 26 (3): 195–209. doi:10.1080/10106049.2010.551669.

Foody, G. M. 2004. "Thematic Map Comparison: Evaluating the Statistical Significance of Differences in Classification Accuracy." *Photogrammetric Engineering and Remote Sensing* 70 (5): 627–634. doi:10.14358/PERS.70.5.627.

Friedman, J. M., G. T. Auble, P. B. Shafroth, M. L. Scott, M. F. Merigliano, M. D. Freehling, and E. R. Griffin. 2005. "Dominance of Non-Native Riparian Trees in Western USA." *Biological Invasions* 7 (4): 747–751. doi:10.1007/s10530-004-5849-z.

Friggens, M. M., and D. M. Finch. 2015. "Implications of Climate Change for Bird Conservation in the Southwestern US Under Three Alternative Futures." *Plos One* 10 (12): e0144089. doi:10.1371/journal.pone.0144089.

Fung, T., and E. LeDrew. 1988. "For Change Detection Using Various Accuracy." *Photogrammetric Engineering and Remote Sensing* 54 (10): 1449–1454.

Gao, B. -C. 1996. "Ndwi—a Normalized Difference Water Index for Remote Sensing of Vegetation Liquid Water from Space." *Remote Sensing of Environment* 58 (3): 257–266. doi:10.1016/S0034-4257(96)00067-3.

Gao, F., and X. Zhang. 2021. "Mapping Crop Phenology in Near Real-Time Using Satellite Remote Sensing: Challenges and Opportunities." *Journal of Remote Sensing*. doi:10.34133/2021/8379391.

Graf, W. L. 1978. "Fluvial Adjustments to the Spread of Tamarisk in the Colorado Plateau Region." *GSA Bulletin* 89 (10): 1491–1501. 10.1130/0016-7606197889<1491:Fattso>2.0.Co;2.

Guo, Y., H. Xia, X. Zhao, L. Qiao, and Y. Qin. 2022. "Estimate the Earliest Phenophase for Garlic Mapping Using Time Series Landsat 8/9 Images." *Remote Sensing* 14 (18): 4476. doi:10.3390/rs14184476.

Hamilton, S. G., S. L. King, G. Dello Russo, and M. D. Kaller. 2019. "Effect of Hydrologic, Geomorphic, and Vegetative Conditions on Avian Communities in the Middle Rio Grande of New Mexico." *Wetlands* 39 (5): 1029–1042. doi:10.1007/s13157-019-01156-9.

Han, H., X. Guo, and H. Yu 2016. "Variable Selection Using Mean Decrease Accuracy and Mean Decrease Gini Based on Random Forest." 2016 7th ieee international conference on software engineering and service science (icsess), Beijing, China.

Hart, C. R., L. D. White, A. McDonald, and Z. Sheng. 2005. "Saltcedar Control and Water Salvage on the Pecos River, Texas, 1999–2003." *Journal of Environmental Management* 75 (4): 399–409. doi:10.1016/j.jenvman.2004.11.023.

Hsu, C. -W., C. -C. Chang, and C. -J. Lin. 2003. *A Practical Guide to Support Vector Classification*. Taiwan: Taipei.

Huang, S., L. Tang, J. P. Hupy, Y. Wang, and G. Shao. 2021. "A Commentary Review on the Use of Normalized Difference Vegetation Index (NDVI) in the Era of Popular Remote Sensing." *Journal of Forestry Research* 32 (1): 1–6. doi:10.1007/s11676-020-01155-1.

Ji, W., and L. Wang. 2015. "Discriminating Saltcedar (Tamarix Ramosissima) from Sparsely Distributed Cottonwood (Populus Euphratica) Using a Summer Season Satellite Image." *Photogrammetric Engineering & Remote Sensing* 81 (10): 795–806. doi:10.14358/PERS.81.10.795.

Ji, W., and L. Wang. 2016. "Phenology-Guided Saltcedar (Tamarix Spp.) Mapping Using Landsat TM Images in Western US." *Remote Sensing of Environment* 173: 29–38. doi:10.1016/j.rse.2015.11.017.

Ji, W., L. Wang, and A. E. Knutson. 2017. "Detection of the Spatiotemporal Patterns of Beetle-Induced Tamarisk (Tamarix Spp.) Defoliation Along the Lower Rio Grande Using Landsat TM Images." *Remote Sensing of Environment* 193: 76–85. doi:10.1016/j.rse.2017.02.019.

Kruse, F. A., A. Lefkoff, J. Boardman, K. Heidebrecht, A. Shapiro, P. Barloon, and A. Goetz. 1993. "The Spectral Image Processing System (Sips)—interactive Visualization and Analysis of Imaging Spectrometer Data." *Remote Sensing of Environment* 44 (2–3): 145–163. doi:10.1016/0034-4257(93)90013-N.

Liu, L., X. Xiao, Y. Qin, J. Wang, X. Xu, Y. Hu, and Z. Qiao. 2020. "Mapping Cropping Intensity in China Using Time Series Landsat and Sentinel-2 Images and Google Earth Engine." *Remote Sensing of Environment* 239: 111624. doi:10.1016/j.rse.2019.111624.

Löw, F., U. Michel, S. Dech, and C. Conrad. 2013. "Impact of Feature Selection on the Accuracy and Spatial Uncertainty of Per-Field Crop Classification Using Support Vector Machines." *Isprs Journal of Photogrammetry and Remote Sensing* 85: 102–119. doi:10.1016/j.isprsjprs.2013.08.007.

Maruthi Sridhar, B. B., R. K. Vincent, W. B. Clapham, S. I. Sritharan, J. Osterberg, C. M. Neale, and D. R. Watts. 2010. "Mapping Saltcedar (Tamarix Ramosissima) and Other Riparian and Agricultural Vegetation in the Lower Colorado River Region Using Multi-Spectral Landsat TM Imagery." *Geocarto International* 25 (8): 649–662. doi:10.1080/10106049.2010.521857.

Masek, J. G., M. A. Wulder, B. Markham, J. McCorkel, C. J. Crawford, J. Storey, and D. T. Jenstrom. 2020. "Landsat 9: Empowering Open Science and Applications Through Continuity." *Remote Sensing of Environment* 248: 111968.

Moon, M., A. D. Richardson, and M. A. Friedl. 2021. "Multiscale Assessment of Land Surface Phenology from Harmonized Landsat 8 and Sentinel-2, PlanetScope, and PhenoCam Imagery." *Remote Sensing of Environment* 266: 112716. doi:10.1016/j.rse.2021.112716.

Nagler, P. L., T. Brown, K. R. Hultine, D. W. Bean, P. E. Dennison, R. S. Murray, E. P. Glenn, and E. P. Glenn. 2012. "Regional Scale Impacts of Tamarix Leaf Beetles (Diorhabda Carinulata) on the Water Availability of Western US Rivers as Determined by Multi-Scale Remote Sensing Methods." *Remote Sensing of Environment* 118: 227–240. doi:10.1016/j.rse.2011.11.011.

Nagler, P. L., E. P. Glenn, C. S. Jarnevich, and P. B. Shafroth. 2011. "Distribution and Abundance of Saltcedar and Russian Olive in the Western United States." *Critical Reviews in Plant Sciences* 30 (6): 508–523. doi:10.1080/07352689.2011.615689.

Nagler, P. L., J. B. Hull, P. B. Shafroth, and C. B. Yackulic 2021. *The Transformation of dryland rivers: The future of introduced tamarisk in the US* (2327-6932).

Narumalani, S., D. R. Mishra, J. Burkholder, P. B. Merani, and G. Willson. 2006. "A Comparative Evaluation of ISODATA and Spectral Angle Mapping for the Detection of Saltcedar Using Airborne Hyperspectral Imagery." *Geocarto International* 21 (2): 59–66. doi:10.1080/10106040608542384.

Niroumand-Jadidi, M., F. Bovolo, M. Bresciani, P. Gege, and C. Giardino. 2022. "Water Quality Retrieval from Landsat-9 (OLI-2) Imagery and Comparison to Sentinel-2." *Remote Sensing* 14 (18): 4596. doi:10.3390/rs14184596.

Pal, M. 2006. "Support Vector Machine-based Feature Selection for Land Cover Classification: A Case Study with DAIS Hyperspectral Data." *International Journal of Remote Sensing* 27 (14): 2877–2894. doi:10.1080/01431160500242515.

Pal, M., and P. M. Mather. 2005. "Support Vector Machines for Classification in Remote Sensing." *International Journal of Remote Sensing* 26 (5): 1007–1011. doi:10.1080/01431160512331314083.

Pan, L., H. Xia, X. Zhao, Y. Guo, and Y. Qin. 2021. "Mapping Winter Crops Using a Phenology Algorithm, Time-Series Sentinel-2 and Landsat-7/8 Images, and Google Earth Engine." *Remote Sensing* 13 (13): 2510. doi:10.3390/rs13132510.

Park, S., J. Im, S. Park, C. Yoo, H. Han, and J. Rhee. 2018. "Classification and Mapping of Paddy Rice by Combining Landsat and SAR Time Series Data." *Remote Sensing* 10 (3): 447. doi:10.3390/rs10030447.

Pettorelli, N., J. O. Vik, A. Mysterud, J. -M. Gaillard, C. J. Tucker, and N. C. Stenseth. 2005. "Using the Satellite-Derived NDVI to Assess Ecological Responses to Environmental Change." *Trends in Ecology & Evolution* 20 (9): 503–510. doi:10.1016/j.tree.2005.05.011.

Phan, T. N., V. Kuch, and L. W. Lehnert. 2020. "Land Cover Classification Using Google Earth Engine and Random Forest Classifier—the Role of Image Composition." *Remote Sensing* 12 (15): 2411. doi:10.3390/rs12152411.

Schmidt, T., C. Schuster, B. Kleinschmit, and M. Förster. 2014. "Evaluating an Intra-Annual Time Series for Grassland Classification—how Many Acquisitions and What Seasonal Origin are Optimal?" *IEEE Journal of Selected Topics in Applied Earth Observations and Remote Sensing* 7 (8): 3428–3439. doi:10.1109/JSTARS.2014.2347203.

Shahfahad, T. S., M. W. Naikoo, A. Gagnon, A. Rahman, A. R. M. T. Islam, A. Mosavi, and A. Mosavi. 2022. "Comparative Evaluation of Operational Land Imager Sensor on Board Landsat 8 and Landsat 9 for Land Use Land Cover Mapping Over a Heterogeneous Landscape." *Geocarto International* 1–21. doi:10.1080/10106049.2022.2152496.

Shen, Y., X. Zhang, W. Wang, R. Nemani, Y. Ye, and J. Wang. 2021. "Fusing Geostationary Satellite Observations with Harmonized Landsat-8 and Sentinel-2 Time Series for Monitoring Field-Scale Land Surface Phenology." *Remote Sensing* 13 (21): 4465. doi:10.3390/rs13214465.

Sheykhmousa, M., M. Mahdianpari, H. Ghanbari, F. Mohammadimanesh, P. Ghamisi, and S. Homayouni. 2020. "Support Vector Machine versus Random Forest for Remote Sensing Image Classification: A Meta-Analysis and Systematic Review." *IEEE Journal of Selected Topics in Applied Earth Observations and Remote Sensing* 13: 6308–6325. doi:10.1109/JSTARS.2020.3026724.

Silván-Cárdenas, J., and L. Wang. 2010. "Retrieval of Subpixel Tamarix Canopy Cover from Landsat Data Along the Forgotten River Using Linear and Nonlinear Spectral Mixture Models." *Remote Sensing of Environment* 114 (8): 1777–1790. doi:10.1016/j.rse.2010.04.003.

Tai, X., and L. Wang. 2014. "Develop an Ensemble Support Vector Data Description Method for Improving Invasive Tamarisk Mapping at Regional Scale." *International Journal of Remote Sensing* 35 (19): 7030–7045. doi:10.1080/01431161.2014.965283.

Wang, L., J. L. Silván-Cárdenas, J. Yang, and A. E. Frazier. 2013. "Invasive Saltcedar (Tamarisk Spp.) Distribution Mapping Using Multiresolution Remote Sensing Imagery." *The Professional Geographer* 65 (1): 1–15. doi:10.1080/00330124.2012.679440.

Wang, J., X. Xiao, L. Liu, X. Wu, Y. Qin, J. L. Steiner, and J. Dong. 2020. "Mapping Sugarcane Plantation Dynamics in Guangxi, China, by Time Series Sentinel-1, Sentinel-2 and Landsat Images." *Remote Sensing of Environment* 247: 111951. doi:10.1016/j.rse.2020.111951.

Wang, L., and S. Zhang. 2014. "Incorporation of Texture Information in a SVM Method for Classifying Salt Cedar in Western China." *Remote Sensing Letters* 5 (6): 501–510. doi:10.1080/2150704X.2014.928422.

Xun, L., and L. Wang. 2015. "An Object-Based SVM Method Incorporating Optimal Segmentation Scale Estimation Using Bhattacharyya Distance for Mapping Salt Cedar (Tamarisk Spp.) with QuickBird Imagery." *GIScience & Remote Sensing* 52 (3): 257–273. doi:10.1080/15481603.2015.1026049.

Yang, C., J. H. Everitt, and R. S. Fletcher. 2013. "Evaluating Airborne Hyperspectral Imagery for Mapping Saltcedar Infestations in West Texas." *Journal of Applied Remote Sensing* 7 (1): 073556. doi:10.1117/1.JRS.7.073556.

You, H., X. Tang, W. Deng, H. Song, Y. Wang, and J. Chen. 2022. "A Study on the Difference of LULC Classification Results Based on Landsat 8 and Landsat 9 Data." *Sustainability* 14 (21): 13730. doi:10.3390/su142113730.

Zhang, X., X. Xiao, S. Qiu, X. Xu, X. Wang, Q. Chang, J. Wu, and B. Li. 2022. "Quantifying Latitudinal Variation in Land Surface Phenology of Spartina Alterniflora Saltmarshes Across Coastal Wetlands in China by Landsat 7/8 and Sentinel-2 Images." *Remote Sensing of Environment* 269: 112810. doi:10.1016/j.rse.2021.112810.